minerals

MDPI

Article

Iron–Titanium Oxide–Apatite–Sulfide–Sulfate Microinclusions in Gabbro and Adakite from the Russian Far East Indicate Possible Magmatic Links to Iron Oxide–Apatite and Iron Oxide–Copper–Gold Deposits

Pavel Kepezhinskas *, Nikolai Berdnikov, Valeria Krutikova and Nadezhda Kozhemyako

Institute of Tectonics and Geophysics, Khabarovsk 680000, Russia; nick@itig.as.khb.ru (N.B.); nm32697@gmail.com (V.K.); nadezdavitman78925@gmail.com (N.K.)
* Correspondence: pavel_k7@yahoo.com

Abstract: Mesozoic gabbro from the Stanovoy convergent margin and adakitic dacite lava from the Pliocene–Quaternary Bakening volcano in Kamchatka contain iron–titanium oxide–apatite–sulfide–sulfate (ITOASS) microinclusions along with abundant isolated iron–titanium minerals, sulfides and halides of base and precious metals. Iron–titanium minerals include magnetite, ilmenite and rutile; sulfides include chalcopyrite, pyrite and pyrrhotite; sulfates are represented by barite; and halides are predominantly composed of copper and silver chlorides. Apatite in both gabbro and adakitic dacite frequently contains elevated chlorine concentrations (up to 1.7 wt.%). Mineral thermobarometry suggests that the ITOASS microinclusions and associated Fe-Ti minerals and sulfides crystallized from subduction-related metal-rich melts in mid-crustal magmatic conduits at depths of 10 to 20 km below the surface under almost neutral redox conditions (from the unit below to the unit above the QFM buffer). The ITOASS microinclusions in gabbro and adakite from the Russian Far East provide possible magmatic links to iron oxide–apatite (IOA) and iron oxide–copper–gold (IOCG) deposits and offer valuable insights into the early magmatic (pre-metasomatic) evolution of the IOA and ICOG mineralized systems in paleo-subduction- and collision-related geodynamic environments.

Keywords: Stanovoy convergent zone; Kamchatka arc; gabbro; adakite; iron–titanium oxide–apatite–sulfide–sulfate (ITOASS) microinclusions; magmatic crystallization; IOA and IOCG deposits

check for updates

Citation: Kepezhinskas, P.; Berdnikov, N.; Krutikova, V.; Kozhemyako, N. Iron–Titanium Oxide–Apatite–Sulfide–Sulfate Microinclusions in Gabbro and Adakite from the Russian Far East Indicate Possible Magmatic Links to Iron Oxide–Apatite and Iron Oxide–Copper–Gold Deposits. *Minerals* **2024**, *14*, 188. https://doi.org/10.3390/min14020188

Academic Editors: Chao Duan and Wei Li

Received: 29 December 2023
Revised: 8 February 2024
Accepted: 9 February 2024
Published: 11 February 2024

1. Introduction

Iron oxide–apatite (IOA; "Kiruna-type") and iron oxide–copper –gold (IOCG; "Chilean-type") deposits contain major resources of a wide range of critical (iron, copper, phosphorous, rare earths, uranium, etc.) and precious (gold, silver) metals [1–10] and are commonly found in arc-related, orogenic and post-orogenic tectonic settings [1–3,7,11–20]. The formation of most current models involves multi-stage magmatic–hydrothermal processes and hydrous halogen-rich fluids, which scavenge metals from primary mantle-sourced, metal-rich silicate melts [9,21–31]. Evaporitic basin-derived sources were also invoked for ore-forming fluids in some IOCG-IOA systems; for example, the giant Olympic Dam Fe-REE-Cu-Au-U district in Australia, Fe-Cu-Au-mineralized systems in Central Chile and magnetite–apatite deposits along the Middle and Lower Yangtze River in China [6,32–38]. Several IOA and IOCG deposits in orogenic and post-orogenic environments contain magnetite-rich lavas, suggesting the involvement of Fe-rich melts in their formation [10,39–49]. Although these melts occasionally carry a subduction-related geochemical signature, the presence of metal-rich iron oxide–apatite (with carbonate, sulfide and sulfate) melts at convergent margins is poorly documented and their possible sources and modes of origin are still rather inadequately constrained [50–52].

Most studies tend to agree that IOA-IOCG and related mineral systems reflect a complex interplay of crustal magmatic and hydrothermal processes [1–3,5,7,9,10,19,21]. The

occurrence of magnetite lavas with andesitic cement along with cogenetic pyroclastics and even magnetite volcanic bombs [39–41,43,46–48] and the frequent association of IOA-IOCG deposits with plutonic and volcanic rocks of intermediate to felsic compositions (granodiorites and diorites, andesites and dacites) [4,5,10,11,15,20,21] indicate presence of some magmatic component, at least during the early stages of the evolution of IOA, IOCG and related mineral systems. Additional geochemical characteristics such as the Fe isotope signature [29,45] and trace element composition [31] of early-generation magnetite, distribution of F-rich and Cl-rich domains in apatite [28] and Os isotope geochemistry [40] also support petrologic models suggesting that IOA-IOCG deposits can be rooted in evolving lithospheric magmatic systems. On the other hand, evidence for participation of hydrothermal processes appears to be rather overwhelming and, on many occasions, overshadowing presence of magmatic precursors for these extremely complex magmatic-hydrothermal ore environments.

We report a new set of data generated during detailed Scanning Electron Microscopy–Energy-Dispersive Analysis (SEM-EDA) study on two samples representing (1) the plutonic root system of the Stanovoy Suture Zone (SSZ, Mesozoic Stanovoy convergent margin) and (2) Late Cenozoic adakitic dacite lava from the Bakening behind-the-front volcanic complex (BVC) in Kamchatka. The primary goal of this study includes documentation of iron–titanium oxide–apatite–sulfide–sulfate microinclusion assemblages in arc-related plutonic and volcanic rocks with inferences on their igneous origins and possible links to IOCG and IOA deposits. We also hope to shed some new light on the formation of these complicated ore systems and the potential role of magmatic processes in their evolution and genesis.

2. Geologic Background

The Stanovoy Suture Zone is located on the northeastern part of the Central Asian Orogenic Belt and is related to the northward subduction of the Mongol–Okhotsk ocean floor beneath the southern edge of the Siberian Craton [53–55] (Figure 1). The Central Asian Orogenic Belt is composed of various metamorphic, ophiolitic (both MORB and SSZ-types) and arc-related terranes [56–58], some of which were either accreted or subducted along the SSZ in Early Mesozoic [59]. The northward subduction of the Mongol–Okhotsk ocean floor beneath the SSZ is marked, in particular, by mineralized ultramafic-mafic plutonic complexes, which form a linear belt roughly parallel to the southern edge of the Siberian continent [55,60–62]. One of the best developed and certainly most studied (including drilling) intrusions in this magmatic belt is the Ildeus mafic–ultramafic complex, which carries multi-stage polymetallic Ni-Co-Cu-Pt-Pd-Au-Ag mineralization [55,60–62].

The Ildeus mafic–ultramafic intrusion consists of an ultramafic core composed of plagioclase-bearing dunite, harzburgite, lherzolite, wehrlite and websterite rimmed by norite, pyroxene–amphibole gabbro and gabbro-anorthosite. Both mafic and ultramafic rocks are intersected by numerous dikes of clinopyroxenite, websterite, granodiorite and Ti-lamprophyre [55,60–62]. Some core-related ultramafic cumulates and pyroxenitic dikes were locally subjected to several episodes of metasomatism, resulting in hydrated (talc + serpentine + chlorite ± carbonate) and alkali-rich (quartz + albite + potassic feldspar + biotite + sericite ± muscovite) assemblages. Ultramafic rocks display exotic disseminated sulfide-native metal-alloy mineralization [60–62] summarized in Table 1. Ildeus mafic-ultramafic rocks follow a calc-alkaline differentiation trend in AFM diagrams and display prominent high-field-strength element depletions coupled with large-ion lithophile and light rare earth element enrichments characteristic of subduction zone magmas [61,62]. Granodiorites display very low Y concentrations (<10 ppm) and high Sr/Y ratios (50–400) typical of adakites [63–65]. Lamprophyres exhibit high total alkalies, Ti and Nb content, and are classified as arc-related high-Nb basalts [65,66].

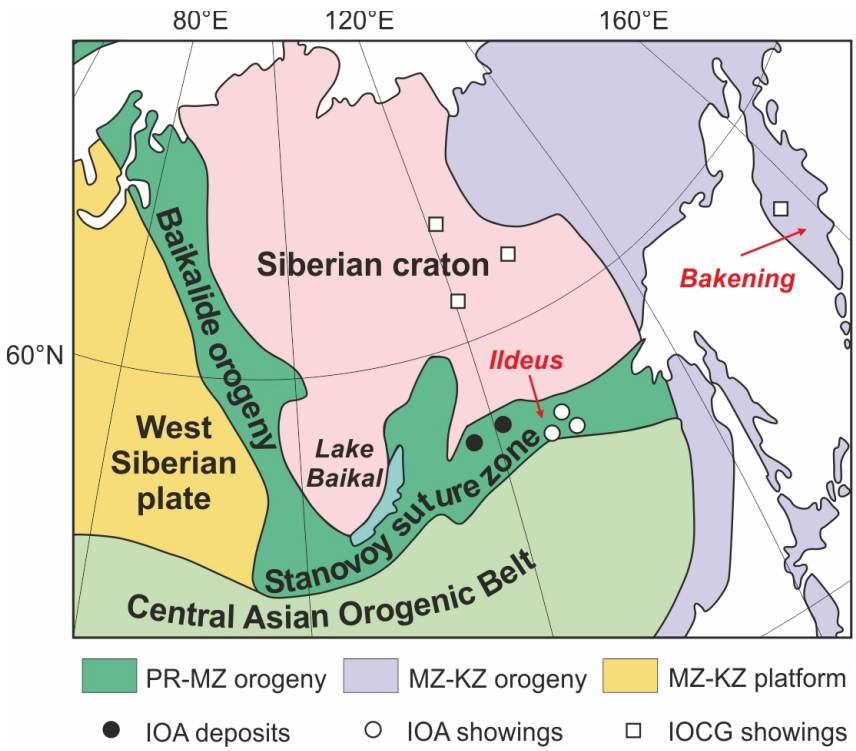

Figure 1. Location of Ildeus mafic–ultramafic arc root complex in the Stanovoy Suture Zone and Bakening volcano in the Kamchatka arc. Map of the main geologic structures and elements of Eastern Siberia and the Russian Far East is modified after [62]. Locations of IOA and IOCG deposits and showings in the Russian Far East are also shown for comparative purposes.

The volcanic province of Kamchatka in the NW corner of the Pacific Ring of Fire records protracted subduction of the Pacific plate beneath Eurasia and consists of three sub-parallel volcanic chains populated by more than 300 active and dormant volcanoes. Most active volcanoes are located in the Eastern Volcanic Front (EVF). The intra-arc rift of the Central Kamchatka Depression, which includes the most productive Eurasian volcano Kluchevskoi, separates the EVF from the Sredinny Range volcanic zone with four active volcanoes [67,68]. The EVF, in turn, is characterized by a complex crustal architecture and includes several cross-arc volcanic chains, such as the Kozelsky–Avachinsky–Koryaksky–Aag–Arik–Kupol–Bakening chain, located just north of the city of Petropavlovsk-Kamchatsky. Bakening is a predominantly andesitic-to-dacitic stratocone built upon older orthopyroxene–clinopyroxene–plagioclase–phyric basaltic andesites and andesites located approximately 110 km to the northwest of the Koryaksky volcano [68,69]. It is composed principally of amphibole–plagioclase–phyric dacites with adakite-like geochemical characteristics (Sr/Y = 30–60) surrounded by primitive olivine–pyroxene basaltic cinder cones and a single mantle xenolith-bearing high-Nb basalt lava flow [68]. Although most volcanic rocks of the Bakening center are consistent with derivation from a variably depleted mantle wedge fluxed by slab fluids [69], the prominent adakitic signature in younger cone dacites and the presence of high-Nb basalt indicates the involvement, however limited, of a slab melt component [68]. A fresh sample of an amphibole–plagioclase–phyric dacite from the main stratocone was selected for our detailed petrologic and SEM-EDA study.

Table 1. Metal and mineral assemblages in the Ildeus mafic–ultramafic intrusion (Stanovoy Suture Zone, Russian Far East).

Metal/Mineral Assemblages/Stages of Evolution	Native Metals	Alloys	Sulfides/Sulfosalts/ Halides/Sulfates/Tellurides	Associated Minerals
Early-stage magmatic	W, Pt, Zn, Bi, Pb, Au	Fe-W, Ti-Co-W, Fe-Pt, Cu-Pt, Ni-Rh-Pt, Pd-Pt, Ni-Cu, Cu-Zn, Cu-Ag, Sn-Zn-Cu, Zn-Cu-Ag, Cu-Ag, Cu-Ag-Au, Cu-Ag-Au-Zn-Ni	Pn, Co-Pn, Po, Mlr, Ccp, Bn, Cu-Ag-S, Fe-Ni-Co-Zn-S, Ag_2S, Brt, Pb-Sn-Cl, AgCl, AgI	Ol, Mg-Opx [(1)], Cpx, Mg-Fe-Cr-Al Spl, Mag, Ilm, Ttn, Rt, Cl-Ap,
Late-stage magmatic	Au	Cu-Ag, Pb-Sb, Ni-Ag-Zn-Cu-Au, Zn-Cu-Au, Cu-Sn	Pn, Po, Ni-Po, Bn, Mlr, Co-Ni-Sp, Co-Ni-Zn-S, Ag_2S, Cu-Ag-Pb-S, Ni-Gn, Sp, Brt	Fe-Opx [(2)], Amp [(3)], Bt, Pl, Mag, Ilm, Ttn, Ap, Bdy, Zrn, Aln, Qz, Cer, Aln, Dol
Metasomatic/Hydrothermal	Ag, Zn, Ni, Au	Cu-Ag-Au, Ag-Au, Cu-Ag, Cu-Zn	Pn, Ccp, Cct, Dg, Hzl, Py, Brt, Cst, Cu-Ag-S, Ag_2S, Gn, Cu-Gn, Sb-Pb-Cl, Ag-Cl-S, Cu-Ag-Cl, AgCl, Bi-Cl, Cu-Sb-Ag-Se-S, Cu-Pb-Fe-As-S, Pb-As-S, Cu-Pb-As-S, Ag_2S, Fe-Cu-Zn-Pb-S, Ni-Zn-Fe-Cu-S, Cu-Ag-Pb-Se-Te,	Tlc, Chl, Srp, Tr, Cb, Ep, Ab, Or, Ba-Or, Qz, Mag, Rt, Ttn, Aln, Mnz, Xtm

Table includes data from [60–62]. [(1)] Mg-rich orthopyroxene (enstatite/bronzite). [(2)] Fe-rich orthopyroxene (hypersthene). [(3)] Al-rich (5–12 wt.% Al_2O_3) pargasitic hornblende [69]. Mineral abbreviations: Ol—olivine, Opx—orthopyroxene, Cpx—clinopyroxene, Pl—plagioclase, Amp—amphibole, Tr—tremolite, Bt—biotite, Ab—albite, Or—orthoclase, Ba-Or—Ba-rich orthoclase, Ep—epidote, Spl—spinel, Mag—magnetite, Ilm—ilmenite, Rt—rutile, Ttn—titanite, Ap—apatite, Cl-Ap—Cl-rich apatite, Bdy—baddeleyite, Zrn—zircon, Aln—allanite, Mnz—monazite, Xtm—xenotime, Cb—carbonates, Cer—cerussite, Dol—dolomite, Pn—pentlandite, Co-Pn—Co-rich pentlandite, Po—pyrrhotite, Ni-Po—Ni-bearing pyrrhotite, Py—pyrite, Ccp—chalcopyrite, Cct—chalcocite, Bn—bornite, Mlr—millerite, Gn—galena, Cu-Gn—Cu-bearing galena, Ni-Gn—Ni-bearing galena, Sp—sphalerite, Co-Ni-Sp—Co- and Ni-bearing sphalerite, Hzl—heazlewoodite, Dg—digenite, Cst—cassiterite.

3. Analytical Methods

Petrographic studies of gabbro from the Ildeus mafic–ultramafic complex and adakitic dacite from the Bakening volcano in Kamchatka were carried out using an Imager A2m petrographic microscope (Carl Zeiss, Jena, Germany).

A comprehensive study of metal and mineral microinclusions in rock-forming minerals in gabbro and adakite was completed using a VEGA 3 LMH TESCAN (TESCAN, Brno, Czech Republic) scanning electron microscope (SEM) with the Oxford X-Max 80 Gb energy-dispersive spectrometer (EDS) (Oxford Instruments, Abingdon, United Kingdom) with the following operating conditions: accelerating voltage of 20 kV, beam current of 530 nA and beam diameter of 0.2 μm. Reference samples including 37 natural and synthetic oxides, minerals and pure native metals (Oxford/108699 no. 6067) were used as standards. Co-standard Oxford Instruments/143100 no. 9864-15 was used for daily calibration of the SEM instrument. The accuracy of the EDS analyses was estimated to be ± 0.1 wt.%. Special sample preparation protocols reported in detail in [70] and designed to prevent contamination were utilized to expose metallic phases in situ and determine their relationships with host silicate and oxide phases as well as associated rock-forming and accessory minerals. Petrographic and SEM studies were completed at the Khabarovsk Innovative Analytical Center (KhIAC) of the Institute of Tectonics and Geophysics, Khabarovsk, Russian Federation.

Microprobe analyses of phenocrysts in adakitic dacite from the Bakening volcano in Kamchatka were carried out using the JEOL-8600 Superprobe at the University of Alabama (Tuscaloosa, AL, USA). Operating conditions were 15 kV accelerating voltage, 20 nA sample current, 40 s maximum counting time and beam diameters of 20 microns for plagioclase and 10 microns for all other mineral phases. A set of natural and synthetic standards was used and the data were processed using the corrections procedure of [71] modified by [72]. Additional details for microprobe procedures used in this study are summarized in [73].

4. Results

Both marginal gabbro from the Triassic Ildeus plutonic root complex in the Stanovoy Suture Zone and adakitic dacite from the Pliocene–Pleistocene Bakening volcano in Kamchatka carry iron–titanium oxide–apatite–sulfide–sulfate (ITOASS) microinclusions in association with a wide range of precious metal minerals and alloys. These mineral assemblages occur in igneous rocks with different textural, mineralogical and geochemical characteristics, which were formed and emplaced within the broad context of a Mesozoic (Ildeus) and Late Cenozoic (Bakening) subduction zone environment.

4.1. Petrology of Gabbro and Adakite

Marginal gabbro in the Ildeus mafic–ultramafic plutonic complex is characterized by a hypidiomorphic–granular texture (Figure 2a) composed of orthopyroxene, clinopyroxene and plagioclase with minor amphibole. Petrographic observations from this marginal gabbro as well as other mafic–ultramafic rocks throughout the Ildeus intrusion [55,62] suggest that Al-rich (SEM-EDA determinations) amphibole is always clearly interstitial (intercumulus, late-stage magmatic; cf. Figure 2c–e in [60]) and never a pyroxene replacement (metasomatic) phase. In fact, all rock-forming minerals in the Ildeus marginal gabbro are quite fresh and do not carry any signs of hydrothermal alteration [62]. Some parts of marginal gabbro display a poikilitic texture with amphibole forming euhedral to subhedral inclusions in calcic plagioclase (Figure 2d in [55]), attesting to the magmatic nature of both silicate minerals. Accessory minerals include abundant apatite, magnetite, ilmenite and sulfide with subordinate zircon, rutile and barite. Sulfides are represented by pentlandite, pyrrhotite, chalcopyrite, Ni-bearing pyrite and pyrite. In some cases, Ni-bearing pyrite appears to form pseudomorphs replacing corroded grains of primary pentlandite. Locally, marginal gabbro from the Ildeus mafic–ultramafic complex is cut by thin (several millimeters to centimeters across) veins of felsic plagioclase-rich material. Geochemical features, especially high Sr/Y (>50) and La/Yb (>30), identify these veins and veinlets as adakite [62]. Adakite veins contain abundant elongated euhedral apatite crystals and minor zircon (Figure 2b).

Adakitic dacite from the Bakening volcano contains euhedral phenocrysts and microphenocrysts of unzoned amphibole, zoned plagioclase and subordinate interstitial quartz and magmatic biotite (Figure 2c,d). Some amphibole grains appear to be corroded and partially abraded (Figure 2c) and most of them are characterized by well-developed opacitic (reaction) rims (Figure 2d), suggesting at least some degree of chemical disequilibria with the surrounding groundmass due to the degassing and slight temperature variations in the ambient melt [74–77]. The groundmass in Bakening adakite displays a classic trachytic texture and is composed of elongated euhedral plagioclase laths, equant Ti-magnetite, quartz, rare ilmenite and potassic feldspar crystals along with varying amounts of silica-rich glass (Figure 2c,d).

Amphibole phenocryst compositions are characterized by relatively high TiO_2 concentrations (1.11–2.66 wt.%; Table 2), high Al_2O_3 content (10.46–12.95 wt.%; Table 2), Mg-numbers of 62.2–71.3 and variable Cr_2O_3 content (0.01–0.20 wt.%; Table 2). Plagioclase compositions vary from An_{45} to An_{94} and all plagioclase phenocrysts contain some iron and, in many cases, very minor but detectable amounts of magnesium and manganese (Table 2). Magnetite contains variable but generally high TiO_2 and V_2O_5 (up to 15 wt.% and 2 wt.%, respectively; Table 2) and is classified as V-bearing titano-magnetite characteristic of subduction-related magmas [78,79]. Ilmenite microphenocrysts and discrete equant grains in the groundmass can be sub-divided into two principal compositional types: (1) relatively MnO-rich and MgO-poor (analysis 12 in Table 2) and (2) relatively MgO-rich (up to 3–4 wt.% MgO) and MnO-poor (analysis 11 in Table 2). While the first type of ilmenite is quite common in evolved island-arc volcanic rocks such as dacites and rhyolites [78–80], the MgO-rich variety is rare and is possibly of a deeper megacrystic (high-pressure phase) or even xenocrystic origin. The elevated geikeilite content of dacitic ilmenites may also

reflect the relatively low oxygen fugacity of magma differentiation as suggested by some experimental data [81].

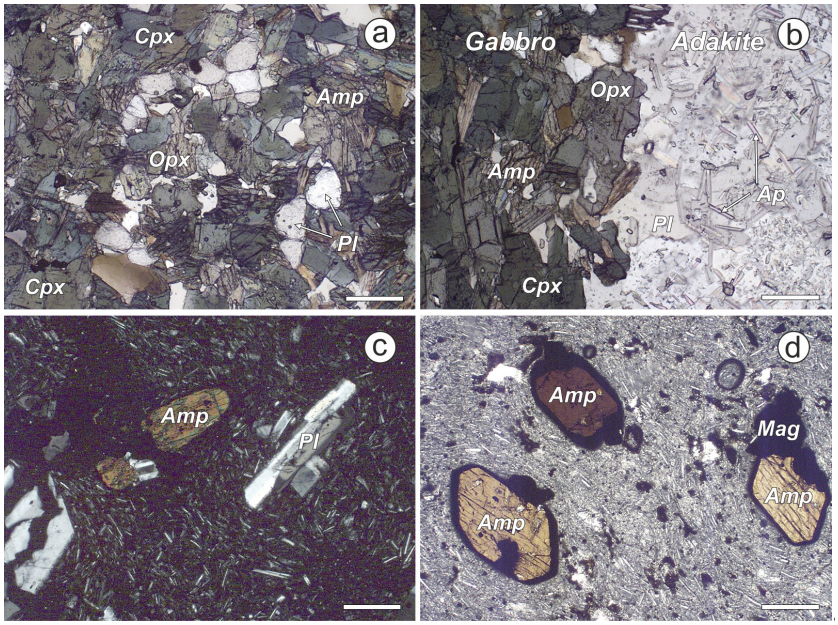

Figure 2. Petrographic features of marginal gabbro from the Ildeus mafic–ultramafic intrusion (**a**,**b**) and adakitic dacite from the Bakening complex (**c**,**d**). (**a**) Hypidiomorphic–granular texture of marginal gabbro (parallel nicols). (**b**) Contact between marginal gabbro and adakite veinlet (parallel nicols). (**c**) Plagioclase-dominated porphyritic texture of the Bakening adakitic dacite (crossed nicols). (**d**) Amphibole-dominated porphyritic texture with trachytic groundmass of the Bakening adakitic dacite (parallel nicols). Opx—orthopyroxene, Cpx—clinopyroxene, Amp—amphibole, Mag—magnetite, Ap—apatite. Scale line 20 μm.

Table 2. Representative phenocryst compositions (wt.%) in the Bakening volcano adakite.

	1	2	3	4	5	6	7	8	9	10	11	12
Mineral	**Amp**	**Amp**	**Amp**	**Amp**	**Amp**	**Amp**	**Pl**	**Pl**	**Mag**	**Mag**	**Ilm**	**Ilm**
SiO_2	45.52	44.29	44.04	46.61	42.98	43.24	49.74	54.41	NA	NA	NA	NA
TiO_2	2.01	2.03	2.08	1.11	2.66	2.30	0.00	0.01	5.63	12.71	44.15	40.34
Al_2O_3	10.87	11.42	11.29	10.46	12.95	12.38	31.39	28.30	3.30	3.01	0.14	0.13
Cr_2O_3	0.08	0.04	0.03	0.01	0.20	0.01	NA	NA	1.46	0.02	0.07	0.01
V_2O_5	NA	NA	NA	NA	NA	NA	NA	NA	0.49	1.11	2.67	2.11
FeO	10.47	11.40	11.70	13.34	10.86	11.35	0.17	0.29	79.55	77.06	46.81	50.05
MnO	0.15	0.15	0.21	0.37	0.16	0.19	0.00	0.01	0.09	0.14	0.34	0.71
MgO	14.39	14.09	14.23	12.33	13.68	14.03	0.01	0.05	3.49	2.90	3.47	1.80
CaO	11.78	11.40	11.11	11.81	10.98	12.09	14.83	10.97	NA	NA	NA	NA
Na_2O	2.01	2.26	2.10	1.87	2.57	2.32	2.86	4.84	NA	NA	NA	NA
K_2O	0.28	0.25	0.29	0.22	0.24	0.27	0.05	0.13	NA	NA	NA	NA
Total	97.56	97.33	97.07	98.14	97.27	100.34	99.05	99.01	94.02	96.95	97.65	95.15
Mg#	71.3	69.8	69.5	62.2	69.2	68.8	-	-	-	-	-	-
An	-	-	-	-	-	-	73.9	55.2	-	-	-	-
P (kb) *	4.8	5.1	5.0	4.8	5.8	5.5	-	-	-	-	-	-

Note. Mg# = Mg/(Mg + Fe). * —Ti-magnetite analysis in Mg-number: Mg/(Mg + Fe) (at.%). NA—not analyzed. Amp—amphibole, Cpx—clinopyroxene, Pl—plagioclase. * P (kbar)—pressure calculated using the empirical Al-in-hornblende geobarometer (Equation (5)) from [77].

Compositions of phenocrystic amphibole in Bakening adakitic dacites range from pargasite through pargasitic and edenitic hornblende to edenite (Figure 3a) chemically similar to amphibole phenocrysts from the Shiveluch volcano adakites in Central Kam-

chatka [82,83]. Plagioclase compositions vary from andesine to almost pure anorthite (Figure 3b). Anorthite megacrysts, frequently in association with Mg-olivine, are found in high-alumina basalts from the Japan [84], Izu–Mariana [85] and Kurile [86] arcs, but are extremely rare in more evolved dacitic-to-rhyolitic magmas [80]. Crystallization pressure for amphibole phenocrysts in Bakening adakite calculated using a refined Al-in-amphibole geobarometer (Equation (5) in [77]) ranges from 4.8 to 5.8 kbar, averaging at around 5 kbar (Table 1). Estimates of oxygen fugacity for the Bakening volcano lavas using Fe-Ti-Mn-Mg oxybarometers developed in [87,88] yielded values of 1–2 units above the quartz–fayalite–magnetite (QFM) buffer. This is similar to the redox conditions (0.5–2.5 units above QFM) typical of modern Kamchatka magmas in particular [89–91] and worldwide arc melts in general [92,93].

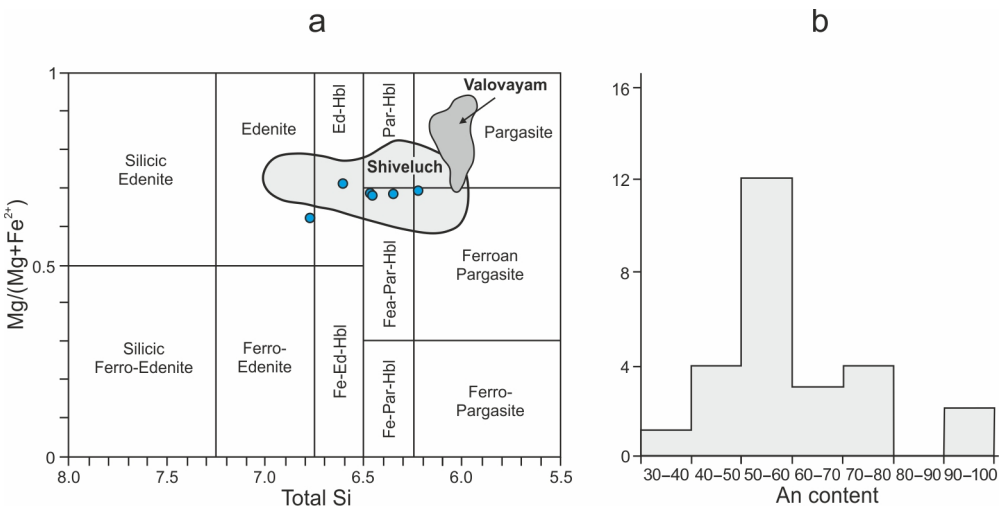

Figure 3. Chemical composition of amphibole (**a**) and plagioclase (**b**) phenocrysts in adakitic dacite from the Bakening volcano (Kamchatka). Fields of amphibole phenocryst compositions in the Shiveluch (Central Kamchatka Depression) and Valovayam (Northern Kamchatka) adakites are based on data from [65,82,83].

4.2. ITOASS Microinclusions in the Ildeus Arc Root Complex (Stanovoy Suture Zone)

Marginal gabbro from the hole ILN-009 in the Ildeus arc root complex contains several quasi-spherical (droplet-like ?) and partially resorbed (multiple textural embayments and locally uneven, undulating contacts with magmatic gabbroic matrix) magmatic segregations typically ranging in size from 0.25 to 5 mm, which are composed of various iron–titanium oxide, apatite, sulfide and sulfate minerals (ITOASS microinclusions; Figure 4). Some well-defined, quasi-spherical segregations have sharp contacts with host late-stage magmatic amphibole (Figure 4a) and contain microinclusions of chalcopyrite along with smaller grains of magnetite, apatite, pyrite and amphibole. Based on the SEM-EDS results, amphiboles inside and outside the ITOASS segregations have slightly different chemical compositions. Primarily, amphibole in the segregations contains elevated Al content (~5–6 wt.%). In comparison, all secondary amphiboles (actinolite, tremolite) with clear replacement textures in the Ildeus complex are characterized by low Al (<2 wt.%) content [55,60–62]. An isolated microinclusion of ilmenite was also observed immediately adjacent to the larger inclusion clusters (Figure 4a), although it is unclear from the textural data if this minute ilmenite could, at some point, have been considered an integral part of the larger ITOASS segregation in Figure 4a.

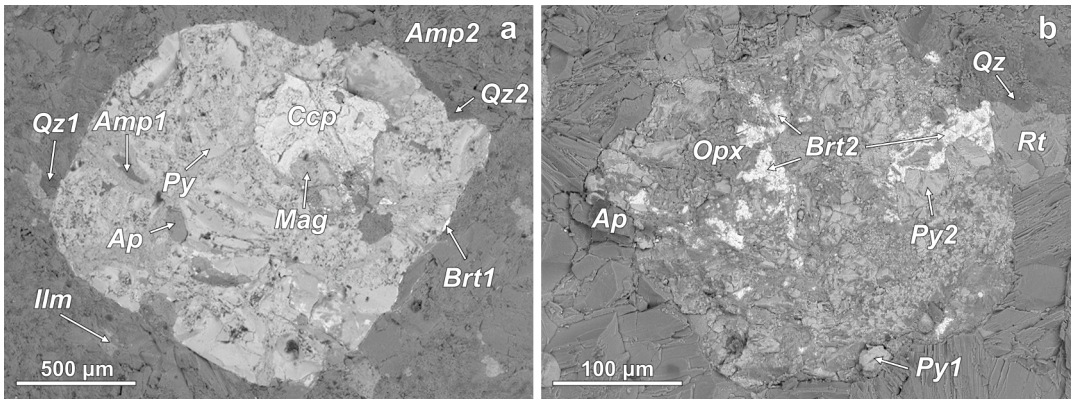

Figure 4. BSE images of quasi-spherical segregations of microinclusions in marginal gabbro from the Ildeus arc root complex. (**a**) Partially deformed and compacted segregation of magnetite, apatite, chalcopyrite, pyrite and barite microinclusions. (**b**) Spherical-type mineral segregation composed of rutile, apatite, orthopyroxene, pyrite and barite. Opx—orthopyroxene, Amp—amphibole, Qz—quartz, Mag—magnetite, Ilm—ilmenite, Rt—rutile, Ap—apatite, Ccp—chalcopyrite, Py—pyrite, Brt—barite. Original SEM-EDS spectra used for identification of the indexed mineral phases in these BSE images are summarized in Figure S1 (Supplementary Materials).

Other spherical-type microinclusions have slightly more diffuse boundaries with the host gabbroic rock (Figure 4b) and are surrounded by various minerals, including amphibole, plagioclase, apatite, quartz and pyrite. These segregations typically include magnetite, rutile, apatite, pyrite and barite, but may also contain minute crystals of orthopyroxene and amphibole (Figure 4b). Similar minerals, especially magnetite, ilmenite, rutile, apatite and pyrite, are disseminated in the pyroxene–amphibole–plagioclase–quartz gabbroic matrix and may possibly represent disintegrated ITOASS-type microinclusion clusters.

Other types of ITOASS microinclusions in marginal gabbro from ILN-009 are composed of the following mineral assemblages: ilmenite–rutile (Figure 5a), rutile–chalcopyrite–pyrrhotite–pyrite–barite (Figure 5b) and magnetite–chalcopyrite–barite (Figure 5c). These ITOASS assemblages are also found in the Ildeus marginal gabbro together with microinclusions of nickeliferous pyrite (Figure 5d), Cu–Ag–chloride (Figure 5e) and cupriferous silver (Figure 5f).

4.3. ITOASS Microinclusions in the Bakening Volcano (Kamchatka)

Adakitic dacite lava from the Bakening volcano in central Kamchatka contains several inclusions of ilmenite (Figure 6a) and magnetite (Figure 6b) hosted in siliceous glassy groundmass. Both larger ilmenite and magnetite oikocrysts contain euhedral to subhedral oval-shaped apatite microinclusions, which range in size from several microns to 10–15 microns across (Figure 6a,b). Some apatite microinclusions in ilmenite contain up to 0.7 wt.% of chlorine as determined by the SEM-EDA (Figure 6a). Both ilmenite–apatite and magnetite–apatite inclusions in the Bakening adakitic dacite are surrounded by numerous micron-sized magnetite crystallites included in silicic glass (Figure 6a,b).

Ilmenite–magnetite–apatite intergrowths are closely spatially and texturally associated with grains of magnetite and various sulfides (Figure 7). Euhedral to anhedral magnetite crystals ranging in size from 100 to 500 microns are included in amphibole (Figure 7a), primary magmatic biotite (Figure 7b) and K-Na feldspar (Figure 7c). In one particular case, euhedral magnetite contains a minute inclusion of silver chloride and is hosted by amphibole and glassy aphyric groundmass (Figure 7d). In another case, a euhedral magnetite crystal 50 microns across is included in Fe-K-rich glass (Figure 7e), which is also enriched in manganese (0.48 wt.% Mn; SEM-EDA). Another textural type of magnetite in the Bakening adakitic dacite is shown in Figure 7f, where numerous small (about one or two microns in size) euhedral angular-to-roundish magnetite grains are tightly packed into an ovoid-shaped crystalline form along the contact between amphibole and quartz

crystals. This magnetite texture very closely resembles framboidal magnetite aggregations in some sedimentary rocks, where the formation of framboids is believed to be a reflection of changes in the overall redox conditions of mineralization [94].

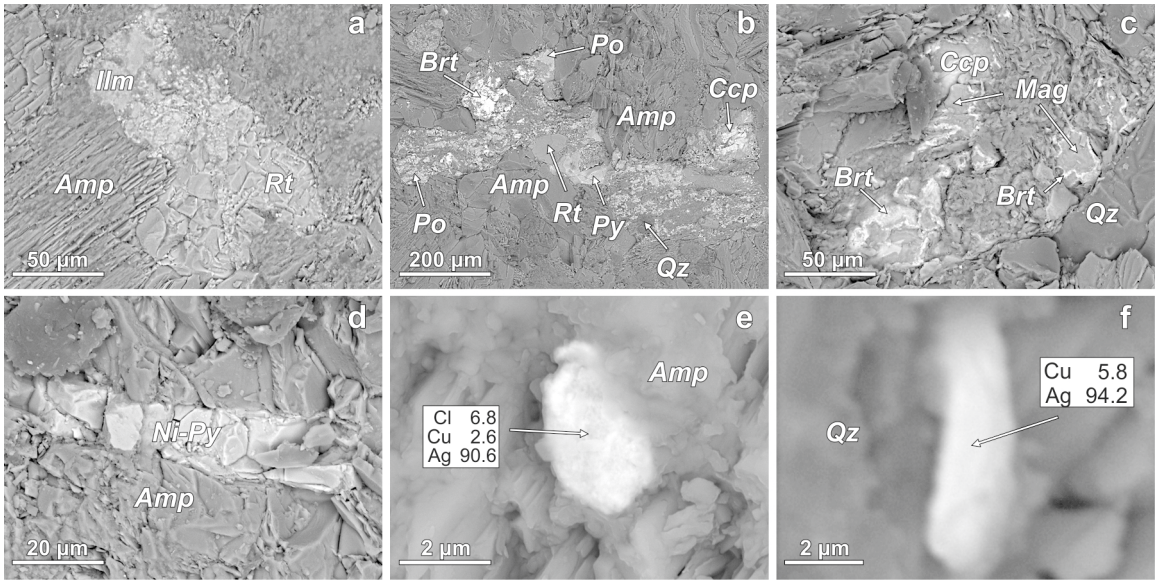

Figure 5. BSE images of microinclusions in marginal gabbro ILN-009 from the Ildeus arc root complex. (**a**) Ilmenite–rutile microinclusion in amphibole. (**b**) Rutile–chalcopyrite–pyrrhotite–pyrite–barite microinclusions in amphibole. (**c**) Magnetite–chalcopyrite–barite microinclusion in quartz–plagioclase–amphibole matrix. (**d**) Euhedral Ni-bearing pyrite microinclusion in amphibole. (**e**) Microinclusion of Cu-Ag-Cl halide in amphibole. (**f**) Microinclusion of cupriferous silver in quartz. Mineral abbreviations: Amp—amphibole, Qz—quartz, Ilm—ilmenite, Rt—rutile, Mag—magnetite, Ccp—chalcopyrite, Py—pyrite, Po—pyrrhotite, Brt—barite.

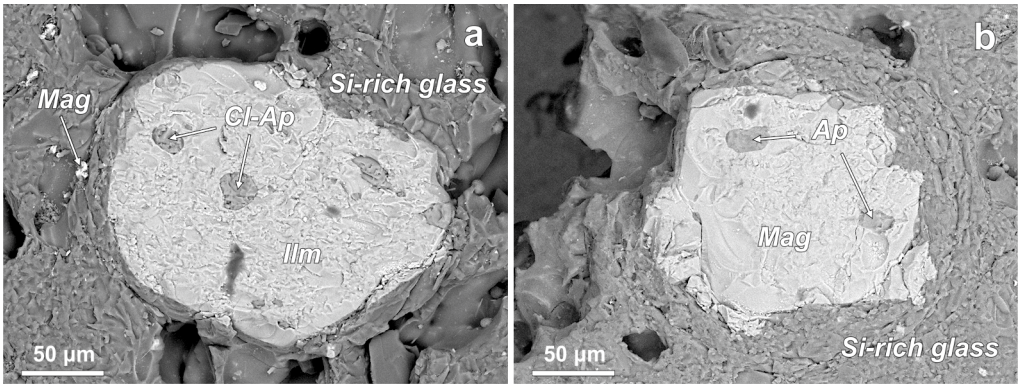

Figure 6. BSE images of iron oxide–apatite inclusions in adakite lava from the Bakening volcano (Kanchatka). (**a**) Ilmenite grain with microinclusions of chlorapatite in association with magnetite in silica-rich glass. (**b**) Magnetite grain with apatite microinclusions in silica-rich glass. Ilm—ilmenite, Mag—magnetite, Cl-Ap—chlorine-bearing (0.7 wt.% of chlorine based on the SEM-EDS analysis) apatite.

Isolated sulfide grains in adakitic dacite lava from the Bakening volcano are less common in comparison with Fe-Ti oxides and are represented by pyrite and acanthite (Figure 8). Pyrite forms equant subhedral to anhedral grains 1 to 5 µm across which are included in quartz–plagioclase groundmass (Figure 8a) or silica-rich residual glass (Figure 8b). Silver sulfide (acanthite Ag_2S) occurs as an anhedral, possibly partially resorbed inclusion in quartz (Figure 8c). In addition, a single anhedral grain of barite approximately 3 microns across is included in quartz microphenocryst (Figure 8d) in the adakitic dacite

lava from the Bakening volcano. Besides pyrite, acanthite and barite, amphibole and plagioclase phenocrysts and groundmass phases in the adakitic lava also contain spongy-like grains and aggregates of non-stoichiometric silver chloride (Figure 8e,f). We have previously shown that the non-stoichiometric ratio of Ag to Cl in the halide microinclusions in magmatic rocks is due to their exposure to light during sample preparation and to electron beams during SEM-EDA studies [61].

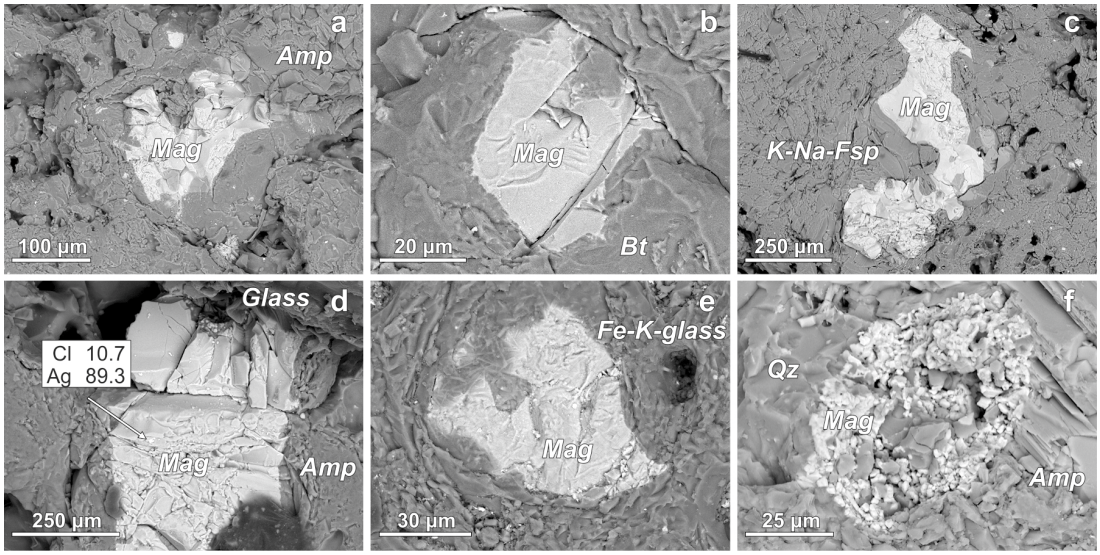

Figure 7. BSE images of magnetite microinclusions in adakitic dacite from the Bakening volcano. (**a**–**c**) Magnetite inclusions in amphibole (**a**), biotite (**b**) and K-Na feldspar (**c**). (**d**) Magnetite inclusion in amphibole and glassy groundmass. (**e**) Magnetite inclusion in Fe-K-rich glass. (**f**) Framboidal-type magnetite aggregate at the contact between amphibole and quartz. Amp—amphibole, Bt—biotite, K-Na Fsp—K-Na feldspar, Qz—quartz, Mag—magnetite.

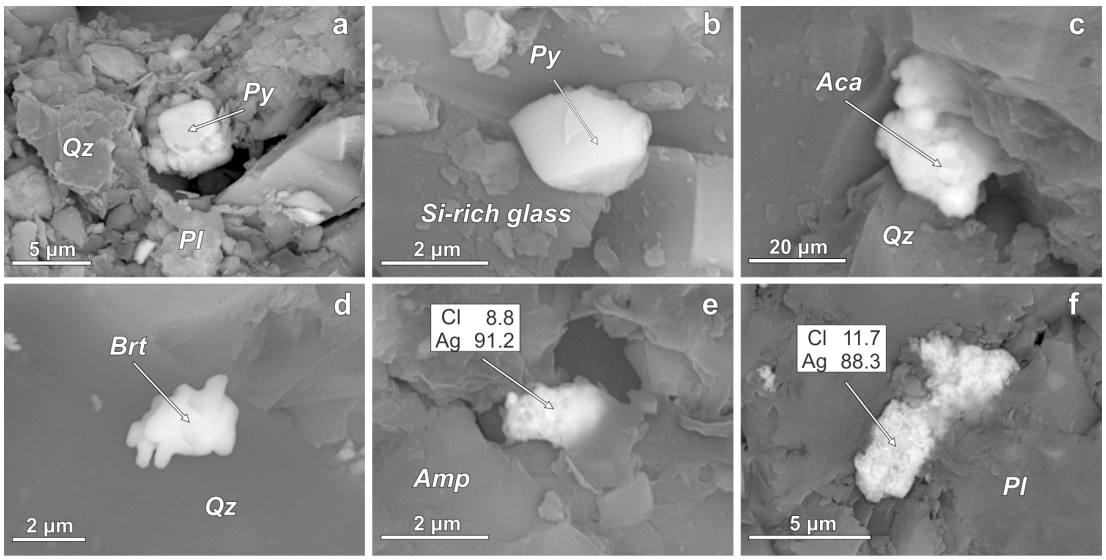

Figure 8. BSE images of sulfide, sulfate and halide microinclusions in adakitic dacite from the Bakening volcano. (**a**) Euhedral pyrite inclusion in the quartz–plagioclase groundmass. (**b**) Subhedral pyrite inclusion in silica-rich groundmass glass. (**c**) Anhedral acanthite (Ag_2S) inclusion in quartz. (**d**) Barite inclusion in quartz microphenocryst. (**e**) Anhedral inclusion of spongy silver chloride in amphibole phenocryst. (**f**) Anhedral aggregate of spongy silver chloride in plagioclase phenocryst. Amp—amphibole, Pl—plagioclase, Qz—quartz, Py—pyrite, Aca—acanthite, Brt—barite.

5. Discussion

Triassic marginal gabbro from the subduction-related mafic–ultramafic plumbing system in the Mesozoic Stanovoy convergent margin and Pliocene–Pleistocene adakites from the Bakening volcano in Kamchatka contain multiple microinclusions of iron–titanium oxide–apatite–sulfide–sulfate (ITOASS) composition. The iron–titanium oxides in the ITOASS are magnetite, ilmenite and rutile, the sulfides are chalcopyrite, pyrite and pyrrhotite, and the sulfate is barite.

ITOASS-type microinclusions in marginal gabbro from the Ildeus mafic–ultramafic arc root complex are characterized by the following mineral assemblages: (1) magnetite–apatite–chalcopyrite–pyrite–pyrrhotite–amphibole–barite; (2) magnetite–apatite–rutile–orthopyroxene–pyrite–barite; (3) rutile–chalcopyrite–pyrrhotite–pyrite–barite; (4) magnetite–chalcopyrite–barite; and (5) ilmenite–rutile (Figures 4 and 5). Although no halogens were detected by SEM-EDA in apatite from the marginal gabbro, apatite in two-pyroxene gabbro, norite, pyroxenite and websterite from the Ildeus complex contained elevated chlorine and fluorine concentrations [55]. The marginal gabbro sample analyzed in this study also contained a single inclusion of Cu–Ag–chloride in amphibole (Figure 5e). Based on the textural and compositional features of ITOASS-bearing magmatic rocks summarized in [55,60–62] along with the occurrence of ITOASS microinclusions in unaltered magmatic rocks, the quasi-spherical shape and sharp contacts with the surrounding magmatic matrix, we infer that the assemblage of magnetite + apatite + ilmenite + chalcopyrite + pyrrhotite + barite I (inclusions inside the ITOASS segregations), along with pentlandite that occurs in some samples containing ITOASS-type associations, is of primary magmatic origin and crystallized from primitive metal-rich subduction-related melt under slightly reduced to slightly oxidized (−1 to +1 ΔQFM mineral buffer) crustal conditions [55,60–62]. It is worth noting here that barite is stable under a wide range of thermodynamic conditions and can be hosted by sedimentary, metamorphic and igneous rocks [95]. Based on the same textural and compositional criteria, mineral association of amphibole + quartz + pyrite + barite II (rims on ITOASS microinclusions and isolated anhedral grains in mafic and ultramafic intrusive rocks) are considered to represent the late magmatic stage in the evolution of the Ildeus magmatic plumbing system [61,62]. It is important to emphasize here that amphibole inside the ITOASS-type clusters appears to contain more Al in comparison with amphibole that hosts the iron–titanium oxide–apatite–sulfide–sulfate microinclusions. This can be interpreted as the reflection of protracted magmatic differentiation history of primary melt that leads to the formation of ITOASS mineral assemblages in the Ildeus arc root mafic–ultramafic complex, as well as similar magmatic hydrothermal systems [62,96,97]. Petrologic conditions of this differentiation inferred from the available mineral compositions and associations, along with the ubiquitous presence of chalcophile metal chlorides and the Cl-rich nature of apatite in the Ildeus arc root complex, suggest that the formation of ITOASS-type microinclusions most probably took place in mid-crustal magmatic plumbing conduits in the presence of a sulfur- and chlorine-rich fluid phase [55,60–62]. It was proposed previously that "IOA deposits typically evolve from subduction-related water-rich and chlorine-rich intermediate magmas under a wide temperature range, almost spanning the whole igneous-hydrothermal spectrum (~1000 to 300 °C)" [19]. Several other studies of well-exposed IOA and IOCG systems also emphasize the importance of chlorine-rich fluids for scavenging and transporting ore metals during the differentiation of primary metal-rich melt and subsequent construction of the upper crustal mineralized magmatic–hydrothermal systems [22–26,30,98–100]. Although the sources of these fluids vary from magmatic mantle- and crustal-derived to basinal evaporitic and meteoric [6,19,22,24], the involvement of sulfur- and chlorine-bearing fluids in the magmatic crystallization of the ITOASS-type microinclusions during development of the Ildeus arc root plutonic complex is well documented and supported by the ubiquitous presence of Cl-rich apatite and copper–silver–lead–antimony–bismuth chlorides in mafic and ultramafic rocks from the Ildeus intrusion [55,60–62].

Iron–titanium oxide–apatite–sulfide–sulfate (ITOASS-type) microinclusions in the adakitic lava from the Bakening volcano are represented by ilmenite–apatite and magnetite–apatite intergrowths (Figure 6) along with isolated individual magnetite and rare ilmenite crystals (Figure 7) in association with pyrite, acanthite and abundant non-stoichiometric silver chloride (Figure 8). Most iron–titanium oxides in the Bakening adakite contain variable V_2O_5 contents (up to 2.8 wt.%) [68,78], potentially indicating substantial variations in redox conditions during the crystallization of the parental subduction-related magmas [101,102]. Apatite microinclusions in ilmenite imbedded in silicic glass from the Bakening adakite (Figure 6a) contain up to 0.7 wt.% of chlorine, suggesting the involvement of Cl-rich fluids in magma genesis and evolution beneath the Bakening volcanic center in the Kamchatka volcanic arc. This is consistent with the ubiquitous presence of silver and silver–copper chloride microinclusions in the Bakening adakitic dacite (Figure 8e,f). Chlorine-rich fluids are integral in promoting the differentiation and evolution of volcanic arc magmas [103–107] and facilitating the transport of ore metals such as copper and gold in crust–mantle systems above active subduction zones [108–110]. High concentrations of chlorine and sulfur have been measured directly in melt inclusions from calc-alkaline lavas [111], as well as in thermal and mineral waters discharged from the volcanic edifices between active volcanoes in Kamchatka [112], suggesting the presence of chlorine-rich fluid in both the mantle wedge and island-arc crust beneath the Kamchatkan volcanic province [65,68,70,113–115].

Ilmenite–apatite and magnetite–apatite microinclusions appear to be in textural equilibrium with residual silicic glass in the adakitic dacite from the Bakening volcano (Figure 6), suggesting crystallization from evolved arc magma within a mid-crustal magma chamber beneath the southern segment of Kamchatka arc. Previous geophysical studies suggested the presence of such magmatic conduits beneath several volcanoes in the vicinity of the Bakening volcanic center, specifically Avachinsky and Koryaksky, located within 100 km to the southeast from the BVC [116,117]. Pressure estimates for the depth of fractionation of parental adakite magma beneath the BVC based on an Al-in-hornblende geobarometer (Table 2) are within 12–17 km, which is consistent with geophysical data from modern Kamchatka volcanoes [117–120] and petrologic constraints from arc-related plutonic complexes exposed at the surface [121–123]. Apatite is a common accessory mineral in most hydrous calc-alkaline magmas [124–126] and, together with magnetite, ilmenite and rutile, is stable under a range of pressures, temperatures and oxygen fugacity values typical of the moderately thick (30–40 km) island-arc crust [127–129]. Experimental and geochemical data suggest that sulfur partitioning between apatite and intermediate to felsic melts in typical crustal volcanic conduits is controlled by decreasing the temperature of crystallization and increasing oxygen fugacity and not so much by the original sulfur enrichment of the parental mantle-derived melt and presence in the fractionating melt of igneous sulfate minerals such as anhydrite [130]. Since no sulfur was detected in either apatite grains from the ITOASS microinclusions or individual apatite crystals in gabbro and adakite from the Russian Far East, we conclude that the decrease in oxygen fugacity during their formation in the crust was negligible and almost all sulfur was partitioned into early magmatic sulfides (pentlandite, pyrrhotite and chalcopyrite in the case of the Ildeus gabbro [55,61,62] and pyrite and acanthite in the case of the Bakening adakite, Figure 8a-c) and late magmatic barite in the case of both Ildeus gabbro (Figure 5b,c) and Bakening adakite (Figure 8d). This interpretation is consistent with the results of Fe-Ti oxide oxybarometry described in Section 4.1 of the Results. Volatile element budgets of apatites in the ITOASS inclusions in both gabbro and adakite from the Russian Far East were controlled by high-temperature hydrous chlorine-rich fluids that assisted differentiation in mid-crustal magmatic conduits and promoted the partitioning of iron, copper, gold, silver and associated critical metals into the later-stage exsolved mineralizing fluids associated with IOA and IOCG systems [7–10,19,25,29,50–52]. Several iron oxide–apatite deposits are known within the immediate vicinity of the Ildeus intrusion [131] and multiple IOCG mineralized systems were reported from the Aldan shield region north of the SSZ [132] (Figure 1). The presence of

ilmenite–Cl–apatite and magnetite–apatite microinclusions in differentiated siliceous glass in the Bakening lava provides direct evidence for the crystallization of iron oxide–apatite assemblage from evolving adakite melt in a S-Cl-rich-fluid-saturated magmatic conduit beneath an active arc volcano in Kamchatka. If these ITOASS segregations represent actual melts, then we argue that these could give rise to IOA-IOCG systems.

In several cases, magnetite–apatite intrusions and associated IOA deposits are located in the vicinity of each other (e.g., the Ildeus intrusion is surrounded by multiple IOA metal showings; Figure 1) and even interlayered [11,12,133–135], suggesting close spatial, temporal and, perhaps, even genetic link between subduction-related magmas and Kiruna-type mineralization [5,9,20,49,135–138]. Several IOA deposits and showings are known in the vicinity of the Ildeus intrusion in the SSZ and IOCG-type mineralization occurring NW of the Bakening volcano in the Sredinny Range of Kamchatka (Figure 1). Similar geologic, petrologic and metallogenic relationships have been documented in magmatic terranes hosting IOCG deposits in the Andes of South America and elsewhere [1,3,10,13,15,20,139]. Arc-related magmatic roots of IOCG deposits are further emphasized by the frequent occurrence of magnetite lava (similar to the "classic" El Laco locality in northern Chile) in association with magnetite, hematite, chalcopyrite, bornite and gold mineralization [20,39–41,43,47–50], as well as the igneous geochemistry of early generations of magnetite and pyrite in such IOA and IOCG deposits as Carmen, Fresia, El Romeral, El Laco, Los Colorados, Cerro Negro Norte and many others [4,8,18–20,140–144]. We propose that the iron–titanium oxide–apatite–sulfide–sulfate (ITOASS-type) microinclusions in gabbro and adakite from the Russian Far East provide some potential links to the early magmatic stages of formation of IOA and IOCG deposits and offer new insights into the magmatic–hydrothermal evolution of subduction-related mineralized systems in orogenic terranes.

6. Conclusions

1. Mesozoic gabbro from the Stanovoy active margin and Quaternary adakitic dacite lava from the Bakening volcano in Kamchatka contain iron–titanium oxide–apatite–sulfide–sulfate (ITOASS) microinclusions. Iron–titanium oxides are composed of magnetite, ilmenite and rutile; sulfides are composed of chalcopyrite, pyrite and pyrrhotite; and sulfates are represented by barite.
2. Textural and compositional data suggest that ITOASS assemblages crystalized from metal-rich, mantle-derived (Ildeus) or slab-derived (Bakening) fractionating magma at mid-crustal levels (15–20 km below the surface) under slightly reduced to slightly oxidized conditions (from one unit below to one unit above the QFM mineral buffer).
3. Magmatic crystallization and metal mobilization within the ITOASS microinclusions in Stanovoy gabbro and Kamchatka adakite were assisted by S-Cl-rich fluids, as indicated by the presence of Cu–Ag–chlorides in plutonic amphibole and volcanic phenocrysts in adakite lava and the elevated chlorine content of apatite in both gabbro and adakite.
4. Although ITOASS microinclusions in the Stanovoy intrusion were possibly affected by hydrothermal processes during later collision and post-collision tectonic events, primary igneous ITOASS assemblages in the Russian Far East most probably represent the early magmatic roots of some mineralized IOA and IOCG systems.

Supplementary Materials: The following supporting information can be downloaded at: https://www.mdpi.com/article/10.3390/min14020188/s1, Figure S1: SEM-EDS spectra for mineral phases in Figure 4a,b. Mineral abbreviations: Amp—amphibole, Opx—orthopyroxene, Ap—apatite, Ilm—ilmenite, Mag—magnetite, Rt—rutile, Qz—quartz, Ccp—chalcopyrite, Py—pyrite, Brt—barite.

Author Contributions: Conceptualization, P.K. and N.B.; methodology, P.K. and N.B.; software, N.B.; formal analysis, V.K. and N.K.; investigation, P.K., N.B., V.K. and N.K.; resources, N.B.; data curation, P.K., N.B., V.K. and N.K.; writing—original draft preparation, P.K.; writing—review and editing, P.K. and N.B.; visualization, N.B.; supervision, P.K. and N.B.; project administration, P.K.

and N.B.; funding acquisition, N.B. All authors have read and agreed to the published version of the manuscript.

Funding: This study was performed with financial support from the Government of Khabarovsk Region, Russian Federation, grant 44C/2023 18.12.2023.

Data Availability Statement: Data are contained within the article and supplementary materials.

Acknowledgments: We acknowledge detailed comments from the two anonymous reviewers, which substantially improved the first version of this manuscript. We also thank Oleg Alekseenko, Alexander Belousov and Mikhail Zhuravlev for their help in organizing the 2022 drilling campaign at the Ildeus mafic–ultramafic intrusion and in obtaining marginal gabbro samples used in this study.

Conflicts of Interest: The authors declare no conflicts of interest.

References

1. Sillitoe, R. Iron oxide-copper-gold deposits: An Andean view. *Miner. Depos.* **2003**, *38*, 787–812. [CrossRef]
2. Williams, P.; Barton, M.; Fontbote, L.; Mark, G.; Marshick, R. Iron oxide copper-gold deposits: Geology, space-time distribution, and possible modes of origin. *Econ. Geol.* **2005**, *100*, 371–406. [CrossRef]
3. Groves, D.I.; Bierlein, F.P.; Meinert, L.D.; Hitzman, M.W. Iron oxide copper-gold (IOCG) deposits through earth history: Implications for origin, lithospheric setting, and distinction from other epigenetic iron oxide deposits. *Econ. Geol.* **2010**, *105*, 641–654. [CrossRef]
4. Palma, G.; Barra, F.; Reich, M.; Simon, A.C.; Romero, R. A review of magnetite geochemistry of Chilean iron oxide-apatite (IOA) deposits and its implications for ore-forming processes. *Ore Geol. Rev.* **2020**, *126*. [CrossRef]
5. Jonsson, E.; Troll, V.R.; Högdahl, K.; Harris, C.; Weis, F.; Nilsson, K.P.; Skelton, A. Magmatic origin of giant "Kiruna-type" apatite-iron-oxide ores in Central Sweden. *Sci. Rep.* **2013**, *3*, 1644. [CrossRef] [PubMed]
6. Barton, M.D. Iron oxide(-Cu-Au-REE-P-Ag-U-Co) systems. *Treatise Geochem.* **2013**, *13*, 515–541.
7. Simon, A.C.; Knipping, J.; Reich, M.; Barra, F.; Deditius, A.P.; Bilenker, L.; Childress, T. Kiruna-type iron oxide-apatite (IOA) and iron oxide copper-gold (IOCG) deposits form by a combination of igneous and magmatic-hydrothermal processes: Evidence from the Chilean Iron Belt. *SEG Spec. Publ.* **2018**, *21*, 89–114. [CrossRef]
8. Rojas, P.A.; Barra, F.; Deditius, A.; Reich, M.; Simon, A.; Roberts, M.; Rojo, M. New contributions to the understanding of Kiruna-type iron oxide-apatite deposits revealed by magnetite ore and gangue mineral geochemistry at the El Romeral deposit, Chile. *Ore Geol. Rev.* **2018**, *93*, 413–435. [CrossRef]
9. Del Real, I.; Reich, M.; Simon, A.C.; Deditius, A.; Barra, F.; Rodriguez-Mustafa, M.A.; Thompson, J.F.H.; Roberts, M.P. Formation of giant iron oxide-copper-gold deposits by superimposed episodic hydrothermal pulses. *Sci. Rep.* **2023**, *13*, 12041. [CrossRef] [PubMed]
10. Tornos, F.; Velasco, F.; Hanchar, J.M. The magmatic-hydrothermal evolution of the El Laco deposit (Chile) and its implications for the genesis of magnetite-apatite deposits. *Econ. Geol.* **2017**, *112*, 1595–1628. [CrossRef]
11. Badham, J.P.N.; Morton, R.D. Magnetite-apatite intrusions and calc-alkaline magmatism, Camsell River, N.W.T. *Can. J. Earth Sci.* **1976**, *13*, 348–354. [CrossRef]
12. Lyons, J.I. Volcanogenic iron oxide deposits, Cerro de Mercado and vicinity, Durango, Mexico. *Econ. Geol.* **1988**, *83*, 1886–1906. [CrossRef]
13. Hitzman, M.W.; Oreskes, N.; Einaudi, M. Geological characteristics and tectonic setting of Proterozoic iron oxide (Cu U Au REE) deposits. *Precambrian Res.* **1992**, *58*, 241–287. [CrossRef]
14. Bauer, T.E.; Andersson, J.B.H. Regional structural setting of late-orogenic IOCG mineralization along the northern Nautanen deformation zone, Norrbotten, Sweden. *Ore Geol. Rev.* **2023**, *163*. [CrossRef]
15. Ootes, L.; Snyder, D.; Davis, W.J.; Acosta-Góngora, P.; Corriveau, L.; Mumin, A.H.; Gleeson, S.A.; Samson, I.M.; Montreuil, J.F.; Potter, E.; et al. A Paleoproterozoic Andean-type iron oxide copper-gold environment, the Great Bear magmatic zone, Northwest Canada. *Ore Geol. Rev.* **2017**, *81*, 123–139. [CrossRef]
16. Storey, C.D.; Smith, M.P. Metal source and tectonic setting of iron oxide-copper-gold (IOCG) deposits: Evidence from an in situ Nd isotope study of titanite from Norrbotten, Sweden. *Ore Geol. Rev.* **2017**, *81*, 1287–1302. [CrossRef]
17. Parente, C.V.; Verissimo, C.U.V.; Botelho, N.F.; Xavier, R.P.; Menez, J.; de Oliveira Lino, R.; da Silva, C.D.A.; Saraiva dos Santos, T.J. Geology, petrography and mineral chemistry of iron oxide-apatite occurrences (IOA type), western sector of the Neoproterozoic Santa Quiteria magmatic arc, Ceará northeast, Brazil. *Ore Geol. Rev.* **2019**, *112*, 103024. [CrossRef]
18. Skirrow, R.J. Iron oxide copper-gold (IOCG) deposits—A review (part 1): Settings, mineralogy, ore geochemistry and classification. *Ore Geol. Rev.* **2022**, *140*, 104569. [CrossRef]
19. Reich, M.; Simon, A.C.; Barra, F.; Palma, G.; Hou, T.; Bilenker, L.D. Formation of iron oxide-apatite deposits. *Nat. Rev. Earth Environ.* **2022**, *3*, 758–775. [CrossRef]
20. Tornos, F.; Hanchar, J.M.; Steele-MacInnis, M.; Crespo, E.; Kamenetsky, V.S.; Casquet, C. Formation of magnetite-(apatite) systems by crystallizing ultrabasic iron-rich melts and slag separation. *Miner. Deposita* **2023**, *59*, 189–225. [CrossRef]

21. Ménard, J.J. Relationship between altered pyroxene diorite and the magnetite mineralization in the Chilean Iron Belt, with emphasis on the El Algarrobo iron deposits (Atacama region, Chile). *Miner. Deposita* **1995**, *30*, 268–274. [CrossRef]
22. Chiaradia, M.; Banks, D.; Cliff, R.; Marschik, R.; De Haller, A. Origin of fluids in iron oxide-copper-gold deposits: Constraints from δ^{37}Cl, ^{87}Sr/^{86}Sr$_i$ and Cl/Br. *Miner. Deposita* **2006**, *41*, 565–573. [CrossRef]
23. Carew, M.J.; Mark, G.; Oliver, N.H.S.; Pearson, N. Trace element geochemistry of magnetite and pyrite in Fe oxide (±Cu-Au) mineralized systems: Insights into the geochemistry of ore-forming fluids. *Geochim. Cosmochim. Acta* **2006**, *70*, A83. [CrossRef]
24. Gleeson, S.A.; Smith, M.P. The sources and evolution of mineralizing fluids in Fe oxide-apatite and iron oxide-copper-gold systems, Norrbotten, Sweden: Constraints from stable Cl isotopes of fluid inclusion leachates. *Geochim. Cosmochim. Acta* **2009**, *73*, 5658–5672. [CrossRef]
25. Smith, M.P.; Gleeson, S.A.; Yardley, B.W.D. Hydrothermal fluid evolution and metal transport in the Kiruna District, Sweden: Contrasting metal behavior in aqueous and aqueous-carbonic brines. *Geochim. Cosmochim. Acta* **2012**, *102*, 89–112. [CrossRef]
26. Bernal, N.F.; Gleeson, S.A.; Smith, M.P.; Barnes, J.D.; Pan, Y. Evidence of multiple halogen sources in scapolites from iron oxide-copper-gold (IOCG) deposits and regional NaCl metasomatic alteration, Norrbotten County, Sweden. *Chem. Geol.* **2017**, *451*, 90–103. [CrossRef]
27. Westhues, A.; Hanchar, J.M.; LeMessurier, M.J.; Whitehouse, M.J. Evidence for hydrothermal alteration and source regions for the Kiruna iron oxide-apatite ore (northern Sweden) from zircon Hf and O isotopes. *Geology* **2017**, *45*, 571–574. [CrossRef]
28. La Cruz, N.L.; Simon, A.C.; Wolf, A.S.; Reich, M.; Barra, F.; Gagnon, S.E. The geochemistry of apatite from the Los Colorados iron oxide-apatite deposit, Chile: Implications for ore genesis. *Miner. Deposita* **2019**, *54*, 1143–1156. [CrossRef]
29. Knipping, J.L.; Fiege, A.; Simon, A.; Oeser, M.; Reich, M.; Bilenker, L. In-situ iron isotope analyses reveal igneous and magmatic-hydrothermal growth of magnetite at the Los Colorados, Kiruna-type iron oxide-apatite deposit, Chile. *Am. Mineral.* **2019**, *104*, 471–484. [CrossRef]
30. Melfou, M.; Richard, A.; Tarantola, A.; Villeneuve, J.; Carr, P.; Peiffert, C.; Mercadier, J.; Dean, B.; Drejing-Carroll, D. Tracking the origin of metasomatic and ore-forming fluids in IOCG deposits through apatite geochemistry (Nautanen North deposit, Norrbotten, Sweden). *Lithos* **2023**, *438–439*, 106995. [CrossRef]
31. Ye, Z.; Mao, J.; Yang, C.; Usca, J.; Li, X. Trace elements in magnetite and origin of the Mariela iron oxide-apatite deposit, Southern Peru. *Minerals* **2023**, *13*, 934. [CrossRef]
32. Oreskes, N.; Einaudi, M.T. Origin of hydrothermal fluids at Olympic Dam: Preliminary results from fluid inclusions and stable isotopes. *Econ. Geol.* **1992**, *87*, 64–90. [CrossRef]
33. Barton, M.D.; Johnson, D.A. Evaporitic-source model for igneous-related Fe-oxide-(REE-Cu-Ag-Au) mineralization. *Geology* **1996**, *24*, 259–262. [CrossRef]
34. Chen, H. External sulphur in IOCG mineralization: Implications on definition and classification of the IOCG clan. *Ore Geol. Rev.* **2013**, *51*, 74–78. [CrossRef]
35. Li, W.; Audétat, A.; Zhang, J. The role of evaporites in the formation of magnetite-apatite deposits along the Middle and Lower Yangtze River, China: Evidence from LA-ICP-MS analysis of fluid inclusions. *Ore Geol. Rev.* **2015**, *67*, 264–278. [CrossRef]
36. Benavides, J.; Kyser, T.K.; Clark, A.H.; Oates, C.J.; Zamora, R.; Tarnovschi, R.; Castillo, B. The Mantoverde iron oxide-copper-gold district, III Región, Chile: The role of regionally derived, nonmagmatic fluids in chalcopyrite mineralization. *Econ. Geol.* **2007**, *102*, 415–440. [CrossRef]
37. Duan, C.; Li, Y.; Mao, J.; Zhu, Q.; Xie, G.; Wan, Q.; Jian, W.; Hou, K. The role of evaporite layers in the ore-forming processes of iron oxide-apatite and skarn Fe deposits: Examples from the middle-lower Yangtze River metallogenic belt, East China. *Ore Geol. Rev.* **2021**, *138*, 104352. [CrossRef]
38. Guo, D.; Li, Y.; Duan, C.; Fan, C. Involvement of evaporite layers in the formation of iron oxide-apatite ore deposits: Examples from the Luohe deposit in China and the El Laco deposit in Chile. *Minerals* **2022**, *12*, 1043. [CrossRef]
39. Park, C.F. A magnetite "flow" in northern Chile. *Econ. Geol.* **1961**, *56*, 431–441. [CrossRef]
40. Barra, F.; Reich, M.; Selbe, D.; Rojas, P.; Simon, A.; Salazar, E.; Palma, G. Unraveling the origin of the Andean IOCG clan: A Re-Os isotope approach. *Ore Geol. Rev.* **2017**, *81*, 62–78. [CrossRef]
41. Henriquez, F.; Martin, R.F. Crystal-growth textures in magnetite flows and feeder dykes, El Laco, Chile. *Can. Mineral.* **1978**, *16*, 581–589.
42. Frietsch, R. On the magmatic origin of iron ores of the Kiruna type. *Econ. Geol.* **1978**, *73*, 478–485. [CrossRef]
43. Travisany, V.; Henriquez, F.; Nyström, J.O. Magnetite lava flows in the Pleito-Melon district of the Chilean Iron Belt. *Econ. Geol.* **1995**, *90*, 438–444. [CrossRef]
44. Chen, H.; Clark, A.H.; Kyser, T.K. The Marcona magnetite deposit, Ica, South-Central Peru: A product of hydrous, iron oxide-rich melts? *Econ. Geol.* **2010**, *105*, 1441–1456. [CrossRef]
45. Troll, V.R.; Weis, F.; Jonsson, E.; Andersson, U.B.; Majidi, S.A.; Högdahl, K.; Harris, C.; Millet, M.-A.; Chinnasamy, S.S.; Koijman, E.; et al. Global Fe-O isotope correlation reveals magmatic origin of "Kiruna-type" apatite-iron oxide ores. *Nat. Commun.* **2019**, *10*, 1712. [CrossRef] [PubMed]
46. Henriquez, F.; Nyström, J.O. Magnetite bombs at El Laco volcano, Chile. *GFF* **1998**, *120*, 269–271. [CrossRef]
47. Nyström, J.O.; Henriquez, F.; Naranjo, J.A.; Naslund, H.R. Magnetite spherules in pyroclastic iron ore at El Laco, Chile. *Am. Mineral.* **2016**, *101*, 587–595. [CrossRef]

48. Velasco, F.; Tornos, F.; Hanchar, J.M. Immiscible iron- and silica-rich melts and magnetite geochemistry at the El Laco volcano (northern Chile): Evidence for a magmatic origin for the magnetite deposits. *Ore Geol. Rev.* **2016**, *79*, 346–366. [CrossRef]
49. Berdnikov, N.V.; Nevstruev, V.G.; Kepezhinskas, P.K.; Krutikova, V.O.; Konovalova, N.S. Silicate, Fe-oxide, and Au-Cu-Ag microspherules in ores and pyroclastic rocks of the Kostenga iron deposit, in the Far East of Russia. *Russ. J. Pacific Geol.* **2021**, *15*, 236–251. [CrossRef]
50. Ovalle, J.T.; La Cruz, N.L.; Reich, M.; Barra, F.; Simon, A.C.; Konecke, B.; Rodriguez-Mustafa, M.A.; Childress, T.; Deditius, A.; Morata, D. Formation of massive iron deposits linked to explosive volcanic eruptions. *Sci. Rep.* **2018**, *8*, 14855. [CrossRef]
51. Bain, W.M.; Steele-MacInnis, M.; Li, K.; Li, L.; Mazdab, F.K.; Marsh, E.E. A fundamental role of carbonate-sulfate melts in the formation of iron oxide-apatite deposits. *Nat. Geosci.* **2020**, *13*, 751–757. [CrossRef]
52. Liedo, H.L.; Naslund, H.R.; Jenkins, D.M. Experiments on phosphate-silicate liquid immiscibility with potential links to iron oxide apatite and nelsonite deposits. *Contrib. Mineral. Petrol.* **2020**, *175*, 111. [CrossRef]
53. Didenko, A.N.; Kaplun, V.B.; Malyshev, Y.F.; Shevchenko, B.F. Lithospheric structure and Mesozoic geodynamics of the eastern Central Asian orogen. *Russ. Geol. Geophys.* **2010**, *51*, 492–506. [CrossRef]
54. Donskaya, T.V.; Gladkochub, D.P.; Mazukabzov, A.M.; Ivanov, A.V. Late Paleozoic-Mesozoic subduction-related magmatism at the southern margin of the Siberian continent and the 150 million-year history of the Mongol-Okhotsk Ocean. *J. Asian Earth Sci.* **2013**, *62*, 79–97. [CrossRef]
55. Kepezhinskas, P.K.; Kepezhinskas, N.P.; Berdnikov, N.V.; Krutikova, V.O. Native metals and intermetallic compounds in subduction-related ultramafic rocks from the Stanovoy mobile belt (Russian Far East): Implications for redox heterogeneity in subduction zones. *Ore Geol. Rev.* **2020**, *127*, 103800. [CrossRef]
56. Kepezhinskas, K.B. Structural-metamorphic evolution of late Proterozoic ophiolites and Precambrian basement in the Central Asian foldbelt of Mongolia. *Precambr. Res.* **1986**, *33*, 209–233. [CrossRef]
57. Safonova, I.; Kotlyarov, A.; Krivonogov, S.; Xiao, W. Intra-oceanic arcs of the Paleo-Asian Ocean. *Gondwana Res.* **2017**, *50*, 167–194. [CrossRef]
58. Furnes, H.; Safonova, I. Ophiolites of the Central Asian Orogenic Belt: Geochemical and petrological characterization and tectonic settings. *Geosci. Front.* **2019**, *10*, 1255–1284. [CrossRef]
59. Natal'in, B.A.; Parfenov, L.M.; Vrublevsky, A.A.; Karsakov, L.P.; Yushmanov, V.V. Main fault systems of the Soviet Far East. *Phil. Trans. R. Soc. Lond.* **1986**, *317*, 267–275.
60. Berdnikov, N.; Kepezhinskas, P.; Konovalova, N.; Kepezhinskas, N. Formation of gold alloys during crustal differentiation of convergent zone magmas: Constraints from an Au-rich websterite in the Stanovoy Suture Zone (Russian Far East). *Geosciences* **2022**, *12*, 126. [CrossRef]
61. Kepezhinskas, P.K.; Berdnikov, N.V. Krutikova, V.O.; Kepezhinskas, N.P.; Astapov, I.A.; Kirichenko, E.A. Silver mineralization in deep magmatogenic systems of ancient island arcs: The Ildeus ultrabasic massif, Stanovoy mobile belt (Russian Far East). *Russ. J. Pacific Geol.* **2023**, *17*, 322–349. [CrossRef]
62. Kepezhinskas, P.; Berdnikov, N.; Kepezhinskas, N.; Krutikova, V.; Astapov, I. Magmatic-hydrothermal transport of metals at arc plutonic roots: Insights from the Ildeus mafic-ultramafic complex, Stanovoy Suture Zone (Russian Far East). *Minerals* **2023**, *13*, 878. [CrossRef]
63. Drummond, M.S.; Defant, M.J.; Kepezhinskas, P.K. Petrogenesis of slab-derived trondhjemite-tonalite-dacite/adakite magmas. *Trans. R. Soc. Edinb.* **1996**, *87*, 205–215.
64. Defant, M.J.; Kepezhinskas, P. Evidence suggests slab melting in arc magmas. *EOS Trans. Amer. Geophys. Union* **2001**, *82*, 65–69. [CrossRef]
65. Kepezhinskas, P. ' Berdnikov, N.; Kepezhinskas, N.; Konovalova, N. Adakites, high-Nb basalts and copper-gold deposits in magmatic arcs and collisional orogens: An overview. *Geosciences* **2022**, *12*, 29. [CrossRef]
66. Kepezhinskas, N.; Kamenov, G.D.; Foster, D.A.; Kepezhinskas, P. Petrology and geochemistry of alkaline basalts and gabbroic xenoliths from Utila Island (Bay Islands, Honduras): Insights into back-arc processes in the Central American Volcanic Arc. *Lithos* **2020**, *352–353*, 105306. [CrossRef]
67. Erlich, E.N.; Gorshkov, G.S. Quaternary volcanism and tectonics in Kamchatka. *Bull. Volcanol.* **1979**, *49*, 13–43.
68. Kepezhinskas, P.; McDermott, F.; Defant, M.J.; Hochstaedter, A.; Drummond, M.S.; Hawkesworth, C.J.; Koloskov, A.; Maury, R.C.; Bellon, H. Trace element and Sr-Nd-Pb isotopic constraints on a three-component model of Kamchatka Arc petrogenesis. *Geochim. Cosmochim. Acta* **1997**, *61*, 577–600. [CrossRef]
69. Dorendorf, F.; Churikova, T.; Koloskov, A.; Wörner, G. Late Pleistocene to Holocene activity at Bakening volcano and surrounding monogenetic centers (Kamchatka): Volcanic geology and geochemical evolution. *J. Volcanol. Geotherm. Res.* **2000**, *104*, 131–151. [CrossRef]
70. Kepezhinskas, P.; Berdnikov, N.; Kepezhinskas, N.; Konovalova, N. Metals in Avachinsky peridotite xenoliths with implications for redox heterogeneity and metal enrichment in the Kamchatka mantle wedge. *Lithos* **2022**, *412–413*, 106610. [CrossRef]
71. Bence, A.E.; Albee, A.L. Empirical correction factors for the electron microanalysis of silicates and oxides. *J. Geol.* **1970**, *76*, 382–403. [CrossRef]
72. Albee, A.L.; Ray, L. Correction factors for electron probe analysis of silicates, oxides, carbonates, phosphates, and sulfates. *Anal. Chem.* **1970**, *42*, 1409–1414. [CrossRef]

73. Kepezhinskas, P.K.; Defant, M.J.; Drummond, M.S. Na metasomatism in the island arc mantle by slab melt-peridotite interaction: Evidence from peridotite xenoliths in the North Kamchatka arc. *J. Petrol.* **1995**, *36*, 1505–1527.
74. Plechov, P.Y.; Tsai, A.E.; Shcherbakov, V.D.; Dirksen, O.V. Opacitization conditions of hornblende in Bezymyannyi volcano andesites (March 30, 1956 eruption). *Petrology* **2008**, *16*, 19–35. [CrossRef]
75. Kiss, B.; Harangi, S.; Ntaflos, T.; Mason, P.R.D.; Pál-Molnár, E. Amphibole perspective to unravel pre-eruptive processes and conditions in volcanic plumbing systems beneath intermediate arc volcanoes: A case study from Ciomadul volcano (SE Carpathians). *Contrib. Mineral. Petrol.* **2014**, *167*, 986. [CrossRef]
76. D'Mello, N.G.; Zelmer, G.F.; Negrini, M.; Kereszturi, G.; Procter, J.; Stewart, R.; Prior, D.; Usuki, M.; Iizuka, Y. Deciphering magma storage and ascent processes of Taranaki, New Zealand, from the complexity of amphibole breakdown textures. *Lithos* **2021**, *398–399*, 106264. [CrossRef]
77. Mutch, E.J.F.; Blundy, J.D.; Tattitch, B.C.; Cooper, F.J.; Brooker, R.A. An experimental study of amphibole stability in low-pressure granitic magmas and a revised Al-in-hornblende geobarometer. *Contrib. Mineral. Petrol.* **2016**, *171*, 85. [CrossRef]
78. Kepezhinskas, P.K. Lateral variations in composition of the minerals along the margin of the Bering Sea. *Int. Geol. Rev.* **1989**, *31*, 680–687. [CrossRef]
79. Bindeman, I.N.; Bailey, J.C. A model of reverse differentiation at Dikii Greben' Volcano, Kamchatka: Progressive basic magma vesiculation in a silicic magma chamber. *Contrib. Mineral. Petrol.* **1994**, *117*, 263–278. [CrossRef]
80. Spiridonov, E.M.; Korotayeva, N.N.; Krivitskaya, N.N.; Ladygin, V.M.; Ovsyannikov, G.N.; Putintseva, E.V.; Semikolennykh, E.S.; Frolova, Y.V. Island-arc augite-bytownite-labradorite dacites of the Kara-Dag massif, Crimea. *Moscow Univer. Geol. Bull.* **2019**, *74*, 582–591. [CrossRef]
81. Evans, B.W.; Scaillet, B. The redox state of Pinatubo dacite and the ilmenite-hematite solvus. *Am. Mineral.* **1997**, *82*, 625–629. [CrossRef]
82. Hartman, M. Characterization and Petrogenesis of Adakitic Pyroclastic Rocks Erupted during the Holocene from Sheveluch Volcano, Kamchatka, Russia. Master's Thesis, New Mexico Institute of Mining and Technology, Socorro, NM, USA, 2002.
83. Gorbach, N.V.; Portnyagin, M.V. Geology and petrology of the lava complex of Young Shiveluch Volcano, Kamchatka. *Petrology* **2011**, *19*, 134–166. [CrossRef]
84. Kimata, M.; Nishida, N.; Shimizu, M.; Saito, S.; Matsui, T.; Arakawa, Y. Anorthite megacrysts from island arc basalts. *Mineral. Mag.* **1995**, *59*, 1–14. [CrossRef]
85. Amma-Miyasaka, M.; Nakagawa, M. Origin of anorthite and olivine megacrysts in island-arc tholeiites: Petrological study of 1940 and 1962 ejecta from Myake-jima volcano, Izu-Mariana arc. *J. Volcanol. Geotherm. Res.* **2002**, *117*, 263–283. [CrossRef]
86. Bindeman, I.N.; Bailey, J.C. Trace elements in anorthite megacrysts from the Kurile Island Arc: A window to across-arc geochemical variations in magma compositions. *Earth Planet. Sci. Lett.* **1999**, *169*, 209–226. [CrossRef]
87. Andersen, D.J.; Lindsley, D.H. Internally consistent solution models for Fe-Mg-Mn-Ti oxides. *Am. Mineral.* **1988**, *73*, 714–726.
88. Arató, R.; Audétat, A. FeTiMM—A new oxybarometer for mafic to felsic magmas. *Geochem. Persp. Let.* **2017**, *5*, 19–23. [CrossRef]
89. Nazarova, D.P.; Portnyagin, M.V.; Krasheninnikov, S.P.; Mironov, N.L.; Sobolev, A.V. Initial H_2O content and conditions of parent magma origin for Gorely volcano (Southern Kamchatka) estimated by trace element thermobarometry. *Dokl. Earth Sci.* **2017**, *472*, 100–103. [CrossRef]
90. Tobelko, D.P.; Portnyagin, M.V.; Krahseninnikov, S.P.; Grib, E.N.; Plechov, P.Y. Compositions and formation conditions of primitive magmas of the Karymsky Volcanic Center, Kamchatka: Evidence from melt inclusions and trace-element thermobarometry. *Petrology* **2019**, *27*, 243–264. [CrossRef]
91. Goltz, A.E.; Krawczynski, M.J.; McCanta, M.C.; Darby Dyar, M. Experimental calibration of an $Fe^{3}+/Fe^{2+}$-in-amphibole oxybarometer and its application to shallow magmatic processes at Shiveluch Volcano, Kamchatka. *Am. Mineral.* **2022**, *107*, 2084–2100. [CrossRef]
92. Kelley, K.A.; Cottrell, E. Water and the oxidation state of subduction zone magmas. *Science* **2009**, *325*, 605–607. [CrossRef]
93. Muth, M.J.; Wallace, P.J. Sulfur recycling in subduction zones and the oxygen fugacity of mafic arc magmas. *Earth Planet. Sci. Lett.* **2022**, *599*, 117836. [CrossRef]
94. Kepezhinskas, P.; Berdnikov, N.; Kepezhinskas, N.; Konovalova, N.; Krutikova, V.; Astapov, I. Nature of Paleozoic basement of the Catalan Coastal Ranges (Spain) and tectonic setting of the Priorat DOQ wine terroir: Evidence from volcanic and sedimentary rocks. *Geosciences* **2023**, *13*, 31. [CrossRef]
95. Hanor, J.S. Barite-celestine geochemistry and environments of formation. *Rev. Mineral. Geochem.* **2000**, *40*, 193–275. [CrossRef]
96. Chen, H.; Clark, A.H.; Kyser, T.K.; Ullrich, T.D.; Baxter, R.; Chen, Y.; Moody, T.C. Evolution of the giant Marcona-Mina Justa iron oxide-copper-gold district, South-Central Peru. *Econ. Geol.* **2010**, *105*, 155–185. [CrossRef]
97. Mateo, L.; Tornos, F.; Hanchar, J.M.; Villa, I.M.; Stein, H.J.; Delgado, A. The Montecristo mining district, northern Chile: The relationships between vein-like magnetite-(apatite) and iron ooxide-copper-gold deposits. *Miner. Depos.* **2023**, *58*, 1023–1049. [CrossRef]
98. Palma, G.; Barra, F.; Reich, M.; Valencia, V.; Simon, A.C.; Vervoort, J.; Leisen, M.; Romero, R. Halogens, trace element cocnetrations, and Sr-Nd isotopes in apatite from iron oxide-apatite (IOA) deposits in the Chilean iron belt: Evidence for magmatic and hydrothermal stages of mineralization. *Geochim. Cosmochim. Acta* **2019**, *246*, 515–540. [CrossRef]

99. Veloso, A.S.R.; Soares Monteiro, L.V.; Juliani, C. The link between hydrothermal nickel mineralization and an iron oxide-copper-gold (IOCG) system: Constraints based on mineral chemistry in the Jatobá deposit, Carajás Province. *Ore Geol. Rev.* **2020**, *121*, 103555. [CrossRef]
100. Sepidbar, F.; Ghorbani, G.; Simon, A.C.; Ma, J.; Palin, R.M.; Homam, S.M. Formation of the Chah-Gaz iron oxide-apatite ore (IOA) deposit, Bafq District, Iran: Constraints from halogens, trace element concentrations, and Sr-Nd isotopes of fluorapatite. *Ore Geol. Rev.* **2022**, *140*, 104599. [CrossRef]
101. Holycross, M.; Cottrell, E. Partitioning of V and 19 other trace elements between rutile and silicate melt as a function of oxygen fugacity and melt composition: Implications for subduction zones. *Am. Mineral.* **2020**, *105*, 244–254. [CrossRef]
102. Shervais, J.W. The petrogenesis of modern and ophiolitic lavas reconsidered: Ti-V and Nb-Th. *Geosci. Front.* **2022**, *13*, 101319. [CrossRef]
103. De Hoog, J.C.M.; Koetsier, G.W.; Bronto, S.; Sriwana, T.; van Bergen, M.J. Sulfur and chlorine degassing from primitive arc magmas: 1982-1983 eruptions of Galunggung (West Java, Indonesia). *J. Volcanol. Geotherm. Res.* **2001**, *108*, 55–83. [CrossRef]
104. Dalou, C.; Koga, K.T.; Le Voyer, M.; Shimizu, N. Contrasting partition behavior of F and Cl during hydrous mantle melting: Implications for Cl/F signature in arc magmas. *Prog. Earth Planet. Sci.* **2014**, *1*, 26. [CrossRef]
105. Zellmer, G.F.; Edmonds, M.; Straub, S.M. Volatiles in subduction zone magmas. *Geol. Soc. Lond. Spec. Publ.* **2014**, *410*, 1–17. [CrossRef]
106. Sharpe, M.S.; Barker, S.J.; Rooyakkers, S.M.; Wilson, C.J.N.; Chambefort, I.; Rowe, M.C.; Schipper, I.; Charlier, B.L.A. A sulfur and halogen budget for the large magmatic system beneath Taupo volcano. *Contrib. Mineral. Petrol.* **2022**, *177*, 95. [CrossRef]
107. Kepezhinskas, P.; Berdnikov, N.; Konovalova, N.; Kepezhinskas, N.; Krutikova, V.; Kirichenko, E. Native metals and alloys in trachytes and shoshonite from the Continental United States and high-K dacite from the Bolivian Andes: Magmatic origins of ore metals in convergent and within-plate tectonic settings. *Russ. J. Pacific Geol.* **2022**, *16*, 405–426. [CrossRef]
108. Tattitch, B.; Chelle-Michou, C.; Blundy, J.; Loucks, R.R. Chemical feedbacks during magma degassing control chlorine partitioning and metal extraction in volcanic arcs. *Nat. Commun.* **2021**, *12*, 1774. [CrossRef] [PubMed]
109. Grondahl, C.; Zajacz, Z. Sulfur and chlorine budgets control the ore fertility of arc magmas. *Nat. Commun.* **2022**, *13*, 4218. [CrossRef] [PubMed]
110. Castillo, P.R. Arc magmatism and porphyry-type ore deposition are primarily controlled by chlorine from seawater. *Chem. Geol.* **2022**, *589*, 120683. [CrossRef]
111. Churikova, T.; Wörner, G.; Mironov, N.; Kronz, A. Volatile (S, Cl and F) and fluid mobile trace element compositions in melt inclusions: Implications for variable fluid sources across the Kamchatka arc. *Contrib. Mineral. Petrol.* **2007**, *154*, 217–239. [CrossRef]
112. Taran, Y.; Ryabinin, G.; Pokrovsky, B.; Malik, N.; Cienfuegos, E. Methane-rich thermal and mineral waters of the Avachinsky Depression, Kamchatka. *Appl. Geochem.* **2022**, *145*, 105414. [CrossRef]
113. Taran, Y.A. Geochemistry of volcanic and hydrothermal fluids and volatile budget of the Kamchatka-Kuril subduction zone. *Geochem. Cosmochim. Acta* **2009**, *73*, 1067–1094. [CrossRef]
114. Dobretsov, N.L.; Koulakov, I.Y.; Litasov, Y.D. Migration paths of magma and fluids and lava compositions in Kamchatka. *Russ. Geol. Geophys.* **2012**, *53*, 1253–1275. [CrossRef]
115. Shu, Y.; Nielsen, S.G.; Le Roux, V.; Wörner, G.; Blusztajn, J.; Auro, M. Sources of dehydration fluids underneath the Kamchatka arc. *Nat. Commun.* **2022**, *13*, 4467. [CrossRef] [PubMed]
116. Moroz, Y.F.; Gontovaya, L.I. Deep structure of the Avacha-Koryakskii volcanic cluster area in Kamchatka. *J. Volcanol. Seismol.* **2003**, *4*, 3–10.
117. Bushenkova, N.; Koulakov, I.; Senyukov, S.; Gordeev, E.I.; Huang, H.-H.; El Khrepy, S.; Al Arifi, N. Tomographic images of magma chambers beneath the Avacha and Koryaksky volcanoes in Kamchatka. *J. Geophys. Res. Solid Earth* **2019**, *124*, 9694–9713. [CrossRef]
118. Steinberg, G.S.; Zubin, M.I. The depth of the magmatic focus under the Avachinsky volcano. *Dokl. Earth Sci.* **1963**, *152*, 968–971.
119. Khubunaya, S.A.; Gontovaya, L.I.; Sobolev, A.V.; Nizkous, I.V. Magma chambers beneath the Klyuchevskoy Volcanic Group (Kamchatka). *J. Volcanol. Seismol.* **2007**, *1*, 98–118. [CrossRef]
120. Ostorero, L.; Balcone-Boissard, H.; Boudon, G.; Shapiro, N.M.; Belousov, A.; Belousova, M.; Auer, A.; Senyukov, S.L.; Droznina, S.Y. Correlated petrology and seismicity indicate indicate rapid magma accumulation prior to eruption of Kizimen volcano, Kamchatka. *Commun. Earth Environ.* **2022**, *3*, 290. [CrossRef]
121. Kepezhinskas, P. Cold Moho boundary beneath island arc systems: An example from the North Kamchatka Arc. *Geophys. Res. Lett.* **1993**, *20*, 2471–2474. [CrossRef]
122. Kepezhinskas, P.; Taylor, R.; Tanaka, H. Geochemistry of plutonic spinels from the North Kamchatka Arc: Comparisons with spinels from other tectonic settings. *Mineral. Mag.* **1993**, *57*, 575–589. [CrossRef]
123. Kepezhinskas, P.K.; Reuber, I.; Tanaka, H.; Miayashita, S. Zoned calc-alkaline plutons in Northeastern Kamchatka, Russia: Implications for the crustal growth in magmatic arcs. *Mineral. Petrol.* **1993**, *49*, 147–174. [CrossRef]
124. Watson, E.B. Apatite saturation in basic to intermediate magmas. *Geophys. Res. Lett.* **1979**, *6*, 937–940. [CrossRef]
125. Green, T.H.; Watson, E.B. Crystallization of apatite in natural magmas under high pressure, hydrous conditions, with particular reference to "Orogenic" rock series. *Contrib. Mineral. Petrol.* **1982**, *79*, 96–105. [CrossRef]
126. Nathwani, C.; Loader, M.A.; Wilkinson, J.J.; Buret, Y.; Sievwright, R.H.; Hollings, P. Multi-stage arc magma evolution recorded by apatite in volcanic rocks. *Geology* **2020**, *48*, 323–327. [CrossRef]

127. Devine, J.D.; Rutherford, M.J.; Norton, G.E.; Young, S.R. Magma storage region processes inferred from geochemistry of Fe-Ti oxides in andesitic magma, Soufrière Hills Volcano, Montserrat, WI. *J. Petrol.* **2003**, *44*, 1375–1400. [CrossRef]
128. Alonzo-Perez, R.; Müntener, O.; Ulmer, P. Igneous garnet and amphibole fractionation in the roots of island arcs: Experimental constraints on andesitic liquids. *Contrib. Mineral. Petrol.* **2009**, *157*, 541–558. [CrossRef]
129. Escuder-Viruete, J.; Castillo-Carrión, M.; Pérez Valera, F.; Valverde-Vaquero, P.; Rubio Ordónez, A.; Fernández, F.J. Reconstructing the crustal section of the intra-oceanic Caribbean island arc: Constraints from the cumulate layered gabbronorites and pyroxenites of the Rio Boba plutonic sequence, Northern Dominican Republic. *Geochem. Geophys. Geosyst.* **2022**, *23*, e2021GC010101. [CrossRef]
130. Parat, F.; Holtz, F. Sulfur partitioning between apatite and melt and effect of sulfur on apatite solubility at oxidizing conditions. *Contrib. Mineral. Petrol.* **2004**, *147*, 201–212. [CrossRef]
131. Kichanova., V.V.; Kichanov, V.D. Gelogical and economic conditions of the Gar iron ore deposit development (Amur region, Russia). In *Mineral Deposit Research: Meeting the Global Challenge*; Mao, J., Bierlein, F.P., Eds.; Springer: Berlin/Heidelberg, Germany, 2005; pp. 135–136.
132. Kostin, A. Iron oxide Cu-Au (IOCG) mineralizing systems: The Eastern Yakutia perspective. *IOP Conf. Ser. Earth Environ. Sci.* **2020**, *609*, 012005. [CrossRef]
133. Hu, L.; Du, Y.-S.; Wang, A.-J.; Yue, Z.-L. Adakitic rocks explained by the deep accumulation of amphibole and apatite near the crust-mantle boundary: A case study from the Tongling region, Lower Yangtze River belt, eastern China. *Geochem. J.* **2017**, *51*, 551–569. [CrossRef]
134. Helvaci, C. Rare earth elements in apatite-rich iron deposits and associated rocks of the Avnik (Bingöl) region, Turkey. *Schweiz. Mineral. Petrogr. Mitt.* **1987**, *67*, 307–319.
135. Hildebrand, R.S. Kiruna-type deposits: Their relationships to intermediate subvolcanic plutons in the Great Bear magmatic zone, northwest Canada. *Econ. Geol.* **1986**, *81*, 640–659. [CrossRef]
136. Esmailiy, D.; Zakizadeh, S.; Sepidbar, F.; Kanaanian, A.; Niroomand, S. The Shaytor apatite-magnetite deposit in the Kashmar-Kerman tectonic zone (Central Iran): A Kiruna-type iron deposit. *Open J. Geol.* **2016**, *6*, 895–910. [CrossRef]
137. Berdnikov, N.; Nevstruev, V.; Kepezhinskas, P.; Astapov, I.; Konovalova, N. Gold in mineralized volcanic systems from the Lesser Khingan Range (Russian Far East): Textural types, composition and possible origins. *Geosciences* **2021**, *11*, 103. [CrossRef]
138. Berdnikov, N.; Kepezhinskas, P.; Nevstruev, V.; Krutikova, V.; Konovalova, N.; Savatenkov, V. Magmatic-hydrothermal origin of Fe-Mn deposits in the Lesser Khingan Range (Russian Far East): Petrographic, mineralogical and geochemical evidence. *Minerals* **2023**, *13*, 1366. [CrossRef]
139. Richards, J.P.; Mumin, A.H. Lithospheric fertilization and mineralization by arc magmas: Genetic links and secular differences between porphyry copper ± molybdenum ± gold and magmatic-hydrothermal iron oxide copper-gold deposits. *Spec. Publ. Soc. Econ. Geol.* **2013**, *17*, 277–300.
140. Dupuis, S.; Beaudoin, G. Discriminant diagrams for iron oxide trace element fingerprinting of mineral deposit types. *Mineral. Deposita* **2011**, *46*, 319–335. [CrossRef]
141. Dare, S.A.S.; Barnes, S.; Beaudoin, G.; Meric, J.; Boutroy, E.; Potvin-Doucet, C. Trace elements in magnetite as petrogenetic indicators. *Miner. Deposita* **2014**, *49*, 785–796. [CrossRef]
142. Knipping, J.L.; Bilenker, L.D.; Simon, A.C.; Reich, M.; Barra, F.; Deditius, A.P.; Wälle, M.; Heinrich, C.A.; Holtz, F.; Munizaga, R. Trace elements in magnetite from massive iron oxide-apatite deposits indicate a combined formation by igneous and magmatic hydrothermal processes. *Geochim. Cosmochim. Acta* **2015**, *171*, 15–38. [CrossRef]
143. Reich, M.; Simon, A.C.; Deditius, A.; Barra, F.; Chryssoulis, S.; Lagas, G.; Tardani, D.; Knipping, J.; Bilenker, L.; Sánchez-Alfaro, P. Trace element signature of pyrite from the Los Colorados iron oxide-apatite (IOA) deposit, Chile: A missing link between Andean IOA and iron oxide copper-gold systems? *Econ. Geol.* **2016**, *111*, 743–761. [CrossRef]
144. Salazar, E.; Barra, F.; Reich, M.; Simon, A.; Leisen, M.; Palma, G.; Romero, R.; Rojo, M. Trace element geochemistry of magnetite from the Cerro Negro Norte iron oxide-apatite deposit, northern Chile. *Miner. Depos.* **2020**, *55*, 409–428. [CrossRef]